







Unveiling the Aromatic and Aliphatic Universe at Redshifts $z \sim 0.2\text{--}0.5$ with JWST/NIRCam

JIANWEI LYU (吕建伟) ¹, XUEJUAN YANG ², AIGEN LI ³, FENGWU SUN ⁴, GEORGE H. RIEKE ⁵, STACEY ALBERTS ⁵,
AND IRENE SHIVAEI ⁶

¹*Steward Observatory, University of Arizona, 933 North Cherry Avenue, Tucson, AZ 85721, USA; jianwei@arizona.edu*

²*Department of Physics, Xiangtan University, 411105 Xiangtan, Hunan Province, China; xjyang@xtu.edu.cn*

³*Department of Physics and Astronomy, University of Missouri, Columbia, MO 65211, USA; lia@missouri.edu*

⁴*Center for Astrophysics | Harvard & Smithsonian, 60 Garden St., Cambridge MA 02138 USA*

⁵*Steward Observatory, University of Arizona, 933 North Cherry Avenue, Tucson, AZ 85721, USA*

⁶*Centro de Astrobiología (CAB), CSIC-INTA, Ctra. de Ajalvir km 4, Torrejón de Ardoz, E-28850, Madrid, Spain*

(Received Feb 20, 2025)

Submitted to ApJ

ABSTRACT

Utilizing deep NIRCam/WFSS data from JWST’s FRESCO program, we spectroscopically survey the $3.3\text{ }\mu\text{m}$ aromatic and $3.4\text{ }\mu\text{m}$ aliphatic C–H stretching emission bands of polycyclic aromatic hydrocarbon (PAH) molecules in galaxies at redshifts $z \sim 0.2\text{--}0.5$. Unlike pre-JWST studies, largely limited to infrared (IR)-bright galaxies ($L_{\text{IR}} \gtrsim 10^{11} L_{\odot}$) at $z \lesssim 0.1$, we probe 200 galaxies down to $L_{\text{IR}} \sim 10^{8.5}\text{--}10^{10} L_{\odot}$ well beyond the local Universe. The $3.3\text{ }\mu\text{m}$ emission is detected at $\geq 3\text{-}\sigma$ in 88 out of 187 galaxies, correlating tightly with galaxy IR luminosity and star formation rate (SFR) and confirming the $3.3\text{ }\mu\text{m}$ PAH as a viable SFR tracer. Despite a large scatter, the $3.3\text{ }\mu\text{m}$ -to-IR luminosity ratio ($L_{3.3}/L_{\text{IR}}$) exhibits a strong metallicity dependence with a drop of $L_{3.3}/L_{\text{IR}}$ by a factor of $\gtrsim 10$ at $12+\log(\text{O}/\text{H}) \sim 8.4\text{--}8.5$ towards lower metallicities. The $3.4\text{ }\mu\text{m}$ emission is detected in 37 out of 159 galaxies, with the $3.4\text{ }\mu\text{m}$ -to- $3.3\text{ }\mu\text{m}$ luminosity ratio ($L_{3.4}/L_{3.3}$) spanning from ~ 0.05 to ~ 0.58 (median ~ 0.19), corresponding to PAH aliphatic fractions of $\sim 0.78\%\text{--}8.3\%$ (median $\sim 2.9\%$) in terms of fractional carbon atoms in aliphatic units. While $L_{3.4}/L_{3.3}$ does not depend significantly on redshift, stellar mass, metallicity, or galaxy morphology, it does decrease with various SFR tracers, suggesting that ultraviolet photons in active star-forming regions may strip aliphatic sidegroups from PAH molecules. Our study showcases the unique power of JWST’s NIRCam/WFSS to systematically map PAH aromatic and aliphatic content in statistically significant, less-biased galaxy samples, providing critical insights into PAH chemistry and its connection to galaxy properties.

1. INTRODUCTION

Polycyclic aromatic hydrocarbon (PAH) molecules are ubiquitous and widespread in the Universe, serving as key tracers of star formation and galaxy evolution. These organic molecules emit distinctive infrared (IR) features at wavelengths of 3.3 , 6.2 , 7.7 , 8.6 , 11.3 and $12.7\text{ }\mu\text{m}$, collectively also known as the “unidentified infrared emission” (UIE) bands (see Tielens 2008; Li 2020). These UIE bands are now commonly believed to arise from the stretching and bending vibrational modes of PAH molecules, which consist of aromatic carbon and hydrogen atoms arranged in benzene ring structures (Leger & Puget 1984; Allamandola et al. 1985). The intensities of these emission bands are tightly correlated with star formation rate (SFR), allowing one to probe star formation activity even in highly obscured environments (e.g., Pope et al. 2008; Shipley et al. 2016; Xie & Ho 2019). Fur-

thermore, PAHs dominate the heating of the interstellar gas by providing photoelectrons and influence the thermal balance and chemistry of the surrounding interstellar medium (ISM; Tielens 2008; Draine & Li 2007). Understanding the nature, origin and evolution of PAHs across cosmic time and galaxy properties offers crucial insights into the interplay between galaxy evolution, dust, and gas.

The $3.3\text{ }\mu\text{m}$ PAH emission band, originating from the aromatic C–H stretches, serves as a critical diagnostic of small, neutral PAHs containing approximately 20–30 carbon atoms (see Draine & Li 2007; Draine et al. 2021). This emission band is sometimes accompanied by a weak satellite emission feature at $3.4\text{ }\mu\text{m}$, which is generally thought to arise from the aliphatic C–H stretch. This implies that astronomical PAHs often include an aliphatic component, e.g., aliphatic sidegroups like methyl ($-\text{CH}_3$) attached as functional groups to PAHs (Yang et al. 2017a; Allamandola et al. 2021). Al-

ternative assignment of the $3.4\ \mu\text{m}$ feature includes anharmonicity (Barker et al. 1987) or superhydrogenation (Bernstein et al. 1996; Sandford et al. 2013; Yang et al. 2020). Despite its potential to reveal critical insights into PAH structure and evolution, the $3.4\ \mu\text{m}$ feature is significantly weaker than the $3.3\ \mu\text{m}$ feature, complicating its detection. Previous extragalactic observations of the $3.4\ \mu\text{m}$ band have primarily been limited to local IR-luminous galaxies and often required high signal-to-noise spectra to confirm its presence (e.g., Imanishi et al. 2010).

With the successful launch and operation of JWST, the study of the 3.3 and $3.4\ \mu\text{m}$ aromatic and aliphatic C–H stretches of PAHs in extragalactic sources has entered a new era. For example, the high-spatial-resolution and sensitive narrow/medium band NIRCam images allow the construction of detailed $3.3\ \mu\text{m}$ PAH emission maps of low- z galaxies up to $z \sim 0.5$ (e.g., Sandstrom et al. 2023; Gregg et al. 2024; Alberts et al. 2024). NIRSpec observations enable the study of the 3.3 and $3.4\ \mu\text{m}$ emission bands along with other molecular and atomic lines well extended into the galactic halo in M82 in great detail (J.W. Lyu et al. in preparation). With the sensitive mid-IR spectral observing capability of MIRI/MRS, the detection of the $3.3\ \mu\text{m}$ PAH emission has been even reported in a gravitationally-lensed galaxy at redshift $z \approx 4.2$ (Spilker et al. 2023), when the Universe was only $\sim 11\%$ of its current age. Based on a MIRI imaging survey, Shivaiei et al. (2024) conducted a systematic study of the evolution of PAH strength from the spectral energy distribution (SED) analysis among galaxies up to cosmic noon, further demonstrating the power of JWST in statistical studies of PAHs.

In this work, we will demonstrate that the Wide-Field Slitless Spectroscopy (WFSS) mode of JWST/NIRCam has also opened new avenues for PAH studies. Unlike targeted observations, WFSS enables blind surveys across large areas of the sky, which capture spectra of all sources within the field of view, offering the opportunity to characterize the PAH behavior in statistically significant and unbiased samples of galaxies. Thanks to the superior sensitivity of NIRCam, with a modest exposure time (~ 1 hr), this allows for the detection of PAH emission in a previously unexplored population of faint galaxies with IR luminosity L_{IR} as low as $10^{8.5} - 10^{10} L_{\odot}$ at $z \lesssim 0.5$, greatly surpassing the limits of earlier AKARI observations with $L_{\text{IR}} > 10^{12} L_{\odot}$ at similar redshifts (e.g., Imanishi et al. 2010; Ichikawa et al. 2014). By covering diverse galaxy populations, including those with very low star formation rates, JWST/NIRCam WFSS broadens the scope of PAH studies, providing a more representative picture of the galaxy population and facilitating comprehensive statistical analyses.

Based on NIRCam/WFSS F444W observations of two GOODS/CANDELS fields, we report here detections of the 3.3 and $3.4\ \mu\text{m}$ PAH emission bands in galaxies at $z \sim$

$0.2 - 0.5$ from the JWST Cycle 1 legacy program FRESCO (First Reionization Epoch Spectroscopically Complete Observations; Oesch et al. 2023). Although FRESCO was designed for the study of very distant Universe, its NIRCam grism observations provide high-quality spectra at $3.8 - 5\ \mu\text{m}$ for objects in the survey footprint, enabling the detection of the $3.3\ \mu\text{m}$ aromatic and weaker $3.4\ \mu\text{m}$ aliphatic C–H stretches, if present, in any galaxies at $z \sim 0.2 - 0.5$ within its survey footprint. In addition, the two fields covered by FRESCO have the most extensive observations across the whole electromagnetic spectrum with both ground-based and space-based facilities over the past two decades, allowing accurate characterizations of various galaxy properties, e.g., stellar population, active galactic nuclei (AGN) content, galaxy morphology, star formation activities in a consistent manner. Thanks to all these, we are able to conduct a comprehensive study on the behaviors of the 3.3 and $3.4\ \mu\text{m}$ PAH emission bands among galaxies with a wide range of properties based on a statistical sample.

We structure this paper as follows. In §2 we briefly describe the data and the sample selection. §3 describes how we conduct various measurements such as the strengths of the 3.3 and $3.4\ \mu\text{m}$ emission bands and put constraints on the galaxy properties. In §4 we explore the behaviors of the 3.3 and $3.4\ \mu\text{m}$ bands and derive the aromatic and aliphatic contents of PAHs and discuss how they vary among galaxy properties (e.g., star formation rates, metallicities, and morphologies). Finally, a summary is given in §5.

Throughout this work, we assume a flat Λ CDM cosmology with $\Omega_m = 0.287$ and $H_0 = 69.3\ \text{km s}^{-1} \text{Mpc}^{-1}$ (Hinshaw et al. 2013).

2. DATA AND SAMPLE SELECTION

2.1. The FRESCO Survey and NIRCam/WFSS Data Reduction

FRESCO is a 53.8 hr medium-sized JWST Cycle 1 legacy program that targets at both the GOODS-S and GOODS-N fields with deep NIRCam/grism WFSS observations. For each field, the NIRCam WFSS observations were conducted to cover a footprint of $62\ \text{arcmin}^2$ in the F444W filter that provides $R \sim 1600$ slitless spectra at $\lambda \sim 3.8 - 5.0\ \mu\text{m}$ for sources within the survey footprint. With an exposure time of ~ 2 hr per pointing, the reached $5\text{-}\sigma$ emission-line sensitivity for compact sources is $\sim 2 \times 10^{-18}\ \text{erg s}^{-1} \text{cm}^{-2}$. In addition to the F444W grism data, NIRCam direct imaging observations in F182M, F210M and F444W with a similar footprint were also obtained. We refer to Oesch et al. (2023) for any additional details about the design and configuration of this program.

We adopted the publicly available NIRCam WFSS data processing routine presented in [Sun et al. \(2023\)](#)¹. Here we only provide a brief summary. In the first round, the data were processed with the standard JWST stage-1 calibration pipeline v1.11.2. For each individual exposure, we assigned world coordinate system (WCS) information, performed flat-fielding, and removed the σ -clipped median sky background.

Given that our sources are reasonably bright and extended, we did not perform any additional background subtraction during the spectral extraction. We optimally extracted 1-D spectra of our targets using their surface brightness profile in the F444W band ([Horne 1986](#)). Since the data are quite deep, contamination from other sources can be seen in many final extracted 2-D and 1-D spectra as evident from the abnormal continuum shape. A detailed contaminant subtraction is very complicated as it requires modeling of the 2-D spectra of $\sim 10^4$ sources across the field, which is beyond the scope of the current paper. As a result, our spectral analysis later will be limited to the sources and wavelength ranges where the contamination is not obvious.

2.2. Sample Selection and Data Collection

In the pre-JWST era, the two GOODS fields have been extensively observed with multi-band images from the ultraviolet (UV) to the mid-IR as well as optical to near-IR spectroscopic follow-ups from both ground-based and space-based missions that allow comprehensive characterizations of the source properties. To construct the parent sample for the FRESCO PAH identifications, we adopted the corresponding 3D-HST catalogs in these fields ([Skelton et al. 2014](#)), which collected the HST/grism redshifts, ground-based spectroscopic redshifts and photometric redshifts. We required the galaxies to have redshifts at $z \sim 0.2$ – 0.45 for the spectral coverage of the $3.3 \mu\text{m}$ PAH feature in the NIRCAM/WFSS F444W filter (~ 3.9 – $5.0 \mu\text{m}$). Within the FRESCO survey footprint, we ended up 200 galaxies with NIRCam/WFSS grism spectra in total with 101 in GOODS-S and 99 in GOODS-N at this redshift range.

In addition to the FRESCO spectral extraction as described in §2.1, we collected various ancillary data for these galaxies to characterize their properties. Besides the ground-based, HST and Spitzer/IRAC photometry at $\lambda \sim 0.3$ – $8.0 \mu\text{m}$ provided by the 3D-HST catalogs, we also cross-matched the sample with available Spitzer/IRS $16 \mu\text{m}$ and Spitzer/MIPS $24 \mu\text{m}$ photometry measurements at longer wavelengths following [Lyu et al. \(2022\)](#) to enable the estimation of galaxy IR luminosity and to improve the identification of obscured AGNs. To estimate the possible AGN contribution in these galaxies, we have matched the sample against the bright AGN catalogs in GOODS-S ([Lyu et al. 2022](#)) and GOODS-

N ([Lyu et al., in prep](#)), which are based on a comprehensive search from the X-ray to the radio bands with the deepest data accessible. Lastly, to characterize the galaxy morphology, we collected the JWST/NIRCam F444W images obtained by the FRESCO program. These images have a PSF FWHM of $0.145''$ corresponding to 0.4 – 0.8 kpc , and cover the rest-frame 3 – $3.7 \mu\text{m}$ for galaxies at $z \sim 0.2$ – 0.45 , allowing a good characterization of most galaxy morphology structures with little dust obscuration.

3. MEASUREMENTS OF GALAXY PROPERTIES AND PAH SPECTRAL PROPERTIES

3.1. Galaxy Properties

The UV to mid-IR SEDs can be used to decipher many key galaxy properties such as star formation history, stellar age, star formation rate, extinction, and possibly as well AGN content. For the SED analysis, we adopted a modified version of *Prospector* ([Johnson et al. 2021](#)) that includes the semi-empirical models of AGN component and galaxy dust emission as detailed in [Lyu et al. \(2024\)](#). For the stellar component, we assumed the Kroupa initial mass function and a delayed- τ star formation history with the [Kriek & Conroy \(2013\)](#) dust attenuation law. For the galaxy dust emission, we adopted the $\log(L_{\text{IR}}/L_{\odot}) = 11.25$ template of [Rieke et al. \(2009\)](#) without the requirement of energy balance. Regarding the AGN component, we used the AGN empirical model with a hybrid extinction law and various narrow and broad emission lines as described in ([Lyu et al. 2024](#)). Readers are highly recommended to check the relevant sections in [Lyu et al. \(2024\)](#) to learn more details about these configurations and justifications. From the SED fittings, we can get useful constraints on the stellar mass (M_{\star}), stellar age (t_{age}), e -folding time for the star formation history (τ_{\star}), dust attenuation level of the stellar continuum ($A_{V,\star}$), and galaxy IR luminosity ($L_{\text{IR,gal}}$). If the AGN contribution is strong with enough SED coverage, AGN properties such as bolometric luminosity (L_{AGN}) and obscuration levels (τ_{IR} , τ_{OPT}) can be also reasonably constrained. In contrast to the original *Prospector* code, we do not introduce energy balance in our fittings.

Due to the complicated nature of AGN and the limitations of the photometry data, SED fittings will not reveal all AGNs in the sample. Luckily, a comprehensive multi-wavelength AGN search in these fields has been carried out by [Lyu et al. \(2022, 2024\)](#) in GOODS-S and by [Lyu et al. \(in preparation\)](#) in GOODS-N. To improve the AGN census, these works utilized the deepest X-ray, optical, mid-IR and radio data available and employed eight selection methods that consider the source X-ray luminosity, X-ray to radio flux ratio, mid-IR color, UV-to-mid-IR SED, radio loudness, radio slope, X-ray/optical variability, spectral emission line properties. We cross-matched our sample of galaxies with these work, and

¹ <https://github.com/fengwusun/nircam-grism>

found 24 AGN candidates in GOODS-S and 11 AGN candidates in GOODS-N. However, most of these AGNs are identified only through the radio-to-X-ray ratio, indicating the AGN is not strong and unlikely influence the PAH behaviors. Eight objects are identified as SED AGNs (as indicated in Table 1), however, their AGN component is obscured at shorter wavelength. None of our sample have been classified as AGN in X-ray. In other words, the AGN contribution to the UV-to-near-IR SED is quite low, so the SED analysis of the galaxy stellar properties are not strongly influenced. Given the lack of strong AGNs in the sample, we will not differentiate objects with and without an AGN.

Although we allow stellar metallicity to vary in our *Prospector* fits, due to its strong degeneracy with stellar population and dust attenuation, the fitted values are not very useful. Direct measurements of gas-phase metallicity requires high-quality rest-frame optical spectra that cover a wide range of wavelength, which are not available for the majority of our sources. Following the strategy described in *Shivaei et al. (2024)*, we estimated metallicities, $12+\log(\text{O}/\text{H})$, with the fundamental metallicity relation (FMR) between stellar mass, SFR, and metallicity as presented in *Sanders et al. (2021)*. For 13 out of 102 GOODS-N galaxies in our sample, we found measurements of their gas-phase metallicity from *Kobulnicky & Kewley (2004)* based on spectral constraints, and these measurements are consistent with the values estimated from FMR within measurement uncertainties.

There are two ways to estimate the galaxy SFRs. Firstly, we can derive the SFR based on the stellar population synthesis results from the *Prospector* SED fittings, assuming a timescale of 10 Myr. The results have been found to be in good agreement with popular SFR tracers such as $\text{H}\alpha$ with a scatter $\lesssim 0.1\text{--}0.2$ dex (*Leja et al. 2017*). Secondly, we can estimate the SFR based on the galaxy IR luminosity following the empirical SFR calibration of *Kennicutt (1998)*. For objects without evidence of AGN from SED analysis, we matched the MIPS $24\mu\text{m}$ photometry by the $\log(L_{\text{IR}}/L_{\odot}) = 11.25$ IR galaxy template of *Rieke et al. (2009)* which has been found to be the best-match of galaxies at higher redshifts (*Rujopakarn et al. 2013*), and compute the total IR luminosity at $8\text{--}1000\mu\text{m}$.² For galaxies without MIPS $24\mu\text{m}$ detection or with an AGN component, we relied on the galaxy IR luminosity derived from the SED fittings where the stellar or AGN contribution at shorter wavelengths is modeled and subtracted. For 91 galaxies, the SED

fitting did not reveal any notable galaxy dust emission and we derived an upper limit of the galaxy IR luminosity by scaling the dust template to the MIPS $24\mu\text{m}$ upper limit. We have compared the IR luminosity values and the SED-derived SFRs and found that they follow closely to the empirical relation described in *Kennicutt & Evans (2012)*.

We made the NIRCam/F444W image cutouts of each galaxy and conducted visual classifications for the galaxy morphology. Following the strategies described in *Kocevski et al. (2015)*, we group the galaxies into six morphology categories: ud – undisturbed disk; dd – disturbed disk; sp – spheroid; ps – point source; ir – irregular; me – merger.

In Table 1, we summarize the various galaxy properties of the sample together with the source ID, redshifts and coordinates in the sky.

To illustrate how our sample differs from previous studies based on AKARI data, we compare in Figure 1 the IR luminosity versus redshift distribution of our selected galaxy sample with that of the AKARI sample (*Imanishi et al. 2010; Ichikawa et al. 2014*). It is clear that the previous AKARI study was largely limited to galaxies at $z \lesssim 0.1$ with very few at $z \sim 0.1\text{--}0.3$. Besides a limited number of galaxies with $\log(L_{\text{IR}}/L_{\odot}) \sim 10\text{--}11$ at very low- z , most of the AKARI galaxies belong to luminous IR galaxies (LIRGs; $\log(L_{\text{IR}}/L_{\odot})=11\text{--}12$) or ultraluminous IR galaxies (ULIRGs; $\log(L_{\text{IR}}/L_{\odot}) > 12$). In contrast, with the deep NIRCam/WFSS data and other multi-wavelength data in these deep fields, we are now able to explore the 3.3 and $3.4\mu\text{m}$ emission bands down to $\log(L_{\text{IR}}/L_{\odot}) \lesssim 11$ statistically at $z \sim 0.2\text{--}0.45$.

3.2. NIRCam/WFSS Spectral Analysis and PAH Feature Characterization

For each source, depending on the wavelength coverage of the usable spectrum, we fit the observed spectrum in terms of one or more Drude profiles combined with an underlying linear continuum:

$$F_{\lambda} = a_0 + a_1\lambda + \sum_j \frac{P_j \times (2\gamma_j/\pi)}{(\lambda - \lambda_{o,j})^2 + \gamma_j^2}, \quad (1)$$

where a_0 and a_1 are the coefficients of the linear continuum; $\lambda_{o,j}$ and γ_j are the central wavelength and width of the j -th Drude profile; P_j , the power emitted from the j -th Drude profile (in unit of $\text{erg s}^{-1} \text{cm}^{-2}$), is obtained by integrating the emission feature over wavelength:

$$P_j = \int_{\lambda_j} \Delta F_{\lambda} d\lambda. \quad (2)$$

As Drude profiles are expected for damping harmonic oscillators, we approximate the 3.3 and $3.4\mu\text{m}$ emission bands as

² 90 galaxies in our sample have *Herschel* far-IR detections (*Elbaz et al. 2011*). However, most of them (69 out of 90) have nearby bright sources that would contaminate the flux measurements, so we decide to use the template-based approach, rather than conducting a complete IR SED fitting throughout the sample.

Table 1. Properties of Galaxies at $z=0.2\text{--}0.5$ within FRESCO footprint

ID	RA	Dec	z	M_*	t_{age}	τ_*	SFR_{SED}	$12+\log(\text{O}/\text{H})$	$\log(L_{\text{IR}}/L_{\odot})$	morphology	AGN?
GS-08629	53.1835632	-27.8621082	0.279	10.98	10.10	5.68	45.51	8.80	11.10	ir	N
GS-09402	53.1703529	-27.8667488	0.359	9.48	2.18	0.82	9.84	8.39	9.35	ud	N
GS-09755	53.1655006	-27.8652668	0.413	9.56	1.31	2.37	2.15	8.60	10.58	me	N
GS-09883	53.1525574	-27.8647594	0.347	9.92	5.64	1.93	12.28	8.56	10.46	ud	N
...

NOTE— Only a portion of this table is shown here to demonstrate its form and content. A machine-readable version of the full table is available online.

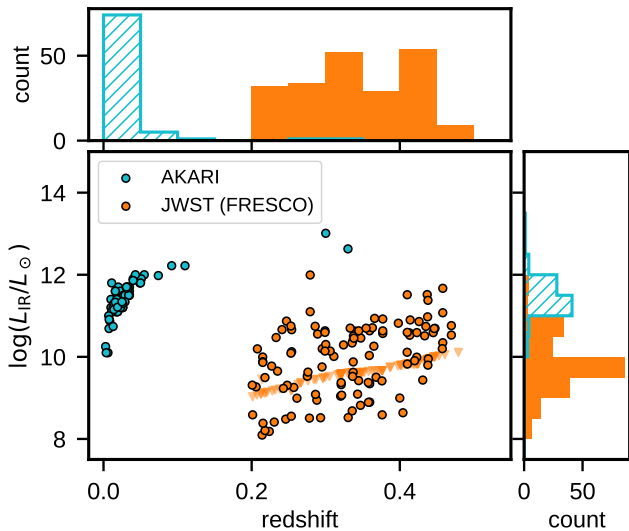


Figure 1. Galaxy IR luminosity versus redshift for the AKARI sample (blue dots; Imanishi et al. 2010; Ichikawa et al. 2014) and the JWST/FRESCO sample in this work (orange dots for galaxies with L_{IR} measurements and orange triangles for galaxies with L_{IR} upper limits).

Drude profiles. In some objects (e.g., GOODS-S 21978), an additional weak band at $\sim 3.47\ \mu\text{m}$ is also present and this band is also included as a Drude profile. In some sources, this $3.47\ \mu\text{m}$ sub-feature appears as a broad plateau, substantially broader than the typical satellite features of the $3.3\ \mu\text{m}$ band at 3.40, 3.43, 3.47, 3.51, and $3.56\ \mu\text{m}$. This $3.47\ \mu\text{m}$ broad plateau appears to correlate with the $3.3\ \mu\text{m}$ band (Pilleri et al. 2015; Lai et al. 2020). In contrast, the $3.47\ \mu\text{m}$ band stands pronouncedly in other sources as a sharp feature, resembling that seen in the planetary nebula IRAS 21282 + 5050 (see Figure 3 of Geballe et al. 1994). In this case, the $3.47\ \mu\text{m}$ band (together with the other weak bands at 3.43, 3.51, and $3.56\ \mu\text{m}$) is generally attributed to aliphatic C–H stretch (see Yang et al. 2017a), although the anharmonicity hypothesis considers all these bands as aromatic (see Barker et al. 1987). Due to this complexity, we

will only count the $3.4\ \mu\text{m}$ emission when we discuss the PAH aliphatic content. Also, the strength of the $3.47\ \mu\text{m}$ feature is sometimes uncertain because of contamination and possible continuum variations.

Due to the nature of slitless spectra, the profile of all these PAH emission bands can be further broadened by the extended galaxy morphology since the PAH emission can come from different locations. As a result, we have convolved all the fitted features with the galaxy 1-D profile along the dispersion direction derived from the F444W image to improve the fittings. We note that the total flux of the band within the aperture would not be affected by this effect once the underlying continuum is properly subtracted.

For all the sources, we have utilized Monte-Carlo methods to produce 1000 mock spectra by perturbing the observed spectrum with the measured $1\text{-}\sigma$ uncertainties. We measured the PAH feature strength in each mock spectrum and compute the standard deviations of the distribution as the measurement uncertainties. In addition, we visually inspected both 2-D and 1-D NIRCам/WFSS spectra and dropped sources with strong nearby source contamination or wavelength coverage too limited for meaningful fittings. In total, we have NIRCам/WFSS spectra of 187 galaxies and 159 galaxies that can be used to constrain the 3.3 and $3.4\ \mu\text{m}$ PAH features.

In Figure 2, we show example FRESCO NIRCам/WFSS spectra and our PAH model fittings for galaxies with different levels of $3.3\ \mu\text{m}$ PAH emission detections. In Table 2, we present the measurements of the PAH emission features from the spectral analysis. In total, we have made $3\text{-}\sigma$ detections of the $3.3\ \mu\text{m}$ feature in 88 galaxies down to $\sim 2.5 \times 10^{-16}\ \text{erg s}^{-1}\ \text{cm}^{-2}$ and the $3.4\ \mu\text{m}$ feature in 37 galaxies down to $\sim 1.8 \times 10^{-16}\ \text{erg s}^{-1}\ \text{cm}^{-2}$. Sources without detections are mostly due to their weak star formation or diffuse emission with the corresponding PAH emission falling below the detection limits.

4. RESULTS AND DISCUSSION

Table 2. Measurements of PAH features at 3.3 and 3.4 μm for galaxies in the FRESCO footprint

ID	z	D	$\lambda_{3.3}$	$P_{3.3}$	$\text{tag}_{3.3}$	$\lambda_{3.4}$	$P_{3.4}$	$\text{tag}_{3.4}$	η_{ali}
		(cm)	(μm)	($\text{erg s}^{-1} \text{cm}^{-2}$)		(μm)	($\text{erg s}^{-1} \text{cm}^{-2}$)		(%)
GS-08629	0.279	4.46E+27	3.284 \pm 0.000	2.10E-15 \pm 6.08E-18	1	3.400 \pm 0.001	4.41E-16 \pm 4.22E-17	1	3.18
GS-09402	0.359	5.99E+27	3.283 \pm 0.001	1.85E-16 \pm 9.57E-18	1	3.416 \pm 0.014	<5.95E-19	1	0.0
GS-09755	0.413	7.06E+27	3.317 \pm 0.011	1.22E-15 \pm 8.54E-17	1	N/A.	N.A.	0	N.A.
GS-09883	0.347	6.08E+27	3.290 \pm 0.000	5.60E-16 \pm 3.19E-17	1	3.406 \pm 0.010	4.75E-17 \pm 4.04E-17	1	1.31
...

NOTE—Here D represent the luminosity distance of the galaxy, $\text{tag}_{3.3}$ and $\text{tag}_{3.4}$ indicate whether the reported measurements can be trusted ($\text{tag} = 1$) or not ($\text{tag} = 0$). Only a portion of this table is shown here to demonstrate its form and content. A machine-readable version of the full table is available online.

With the measurements of the 3.3 and 3.4 μm PAH features in hand, we now explore their behaviors across the sample and assess their connection to galaxy properties.

4.1. The 3.3 μm Aromatic Band

4.1.1. $L_{3.3}$ vs. L_{IR}

A key starting point is to assess the relationship between PAH emission and the total IR luminosity, a well-established tracer of the overall dust heating in galaxies. This analysis provides the foundation for understanding how PAH features evolve across different environments.

In Figure 3, we compare the IR luminosity of the galaxies in our sample with their 3.3 μm PAH luminosity ($L_{3.3} = P_{3.3} \times 4\pi \times d^2$, where d is the galaxy luminosity distance). To extend the dynamical range, we include data from the brighter IR galaxies observed with AKARI (Imanishi et al. 2010; Ichikawa et al. 2014). A strong correlation is evident with a Pearson correlation coefficient of $r \approx 0.71$ and p -value on the order of 10^{-32} . The Spearman test yields $\rho \approx 0.94$ with a p -value of $\sim 10^{-92}$. These results indicate a robust and statistically significant link between $L_{3.3}$ and L_{IR} , suggesting both types of emission originate from heating by UV photons in star-forming regions.

We also found tentative evidence that the ratio $L_{3.3}/L_{\text{IR}}$ may change from $\sim 0.01\%$ at $L_{\text{IR}} \sim 10^{11}\text{--}10^{12.5} L_{\odot}$ to $\sim 0.02\%$ at $L_{\text{IR}} \sim 10^9\text{--}10^{10} L_{\odot}$. This trend mirrors the observed behavior of the other PAH bands, such as the 11.3 μm feature (Lyu & Rieke 2017). Nevertheless, the change of the relative intensity of the 3.3 μm feature is only moderate within the three orders of magnitude variation of L_{IR} , supporting $L_{3.3}$ as a valid tracer of star formation as discussed below.

4.1.2. $L_{3.3}$ vs. SFR

Building on the strong correlation between $L_{3.3}$ and L_{IR} , we now evaluate how the 3.3 μm PAH feature serves as a tracer of star formation activity in galaxies. Adopting the

L_{IR} -calibrated SFR (e.g., Kennicutt & Evans 2012) and the average ratio of $\log(L_{3.3}/L_{\text{IR}}) = -2.77 \pm 0.30$, we can compute the (IR-based) SFR from the 3.3 μm PAH luminosity as

$$\log\left(\frac{\text{SFR}}{M_{\odot} \text{ yr}^{-1}}\right) = \log\left(\frac{L_{3.3}}{L_{\odot}}\right) - (7.03 \pm 0.30) \quad . \quad (3)$$

Meanwhile, we can also use the SED-derived SFR to examine its relation with $L_{3.3}$. As shown in Figure 4, these two independent quantities exhibit a strong correlation. We conduct linear regression analysis in the log-log space with a fixed slope of 1.0 and find the following correlation:

$$\log\left(\frac{L_{3.3}}{L_{\odot}}\right) = \log\left(\frac{\text{SFR}}{M_{\odot} \text{ yr}^{-1}}\right) + (7.17 \pm 0.32) \quad . \quad (4)$$

The scatter is ~ 0.37 . Considering the typical uncertainties of 0.2–0.3 dex of SFR from Prospector, the $L_{3.3}$ –SFR correlation has a $\sim 0.2\text{--}0.3$ dex intrinsic scatter, indicating a tight correlation between $L_{3.3}$ and the SED-derived SFR. The same relation can be rewritten as

$$\log\left(\frac{\text{SFR}}{M_{\odot} \text{ yr}^{-1}}\right) = \log\left(\frac{L_{3.3}}{L_{\odot}}\right) - (7.17 \pm 0.32) \quad . \quad (5)$$

This correlation should be more robust since that the SFR based on SED analysis considers both obscured and unobscured stellar population and the validity of this approach is well-established regardless of the galaxy IR luminosity or stellar mass. In comparison, the L_{IR} -based SFR calibration in Equation 3 is slightly off by ~ 0.14 dex but still within the uncertainty.

Lai et al. (2020) calibrated the 3.3 μm PAH luminosity as a SFR indicator by comparing it to the mid-IR [Ne II] and [Ne III] lines. Compared to that work, for the same 3.3 μm PAH luminosity, the SED-calibrated SFR and the L_{IR} -based SFR would be ~ 0.37 dex and 0.23 dex lower, respectively. These offsets might be explained as a result of systematic differences in SFR calibration, adopted methodology as well as

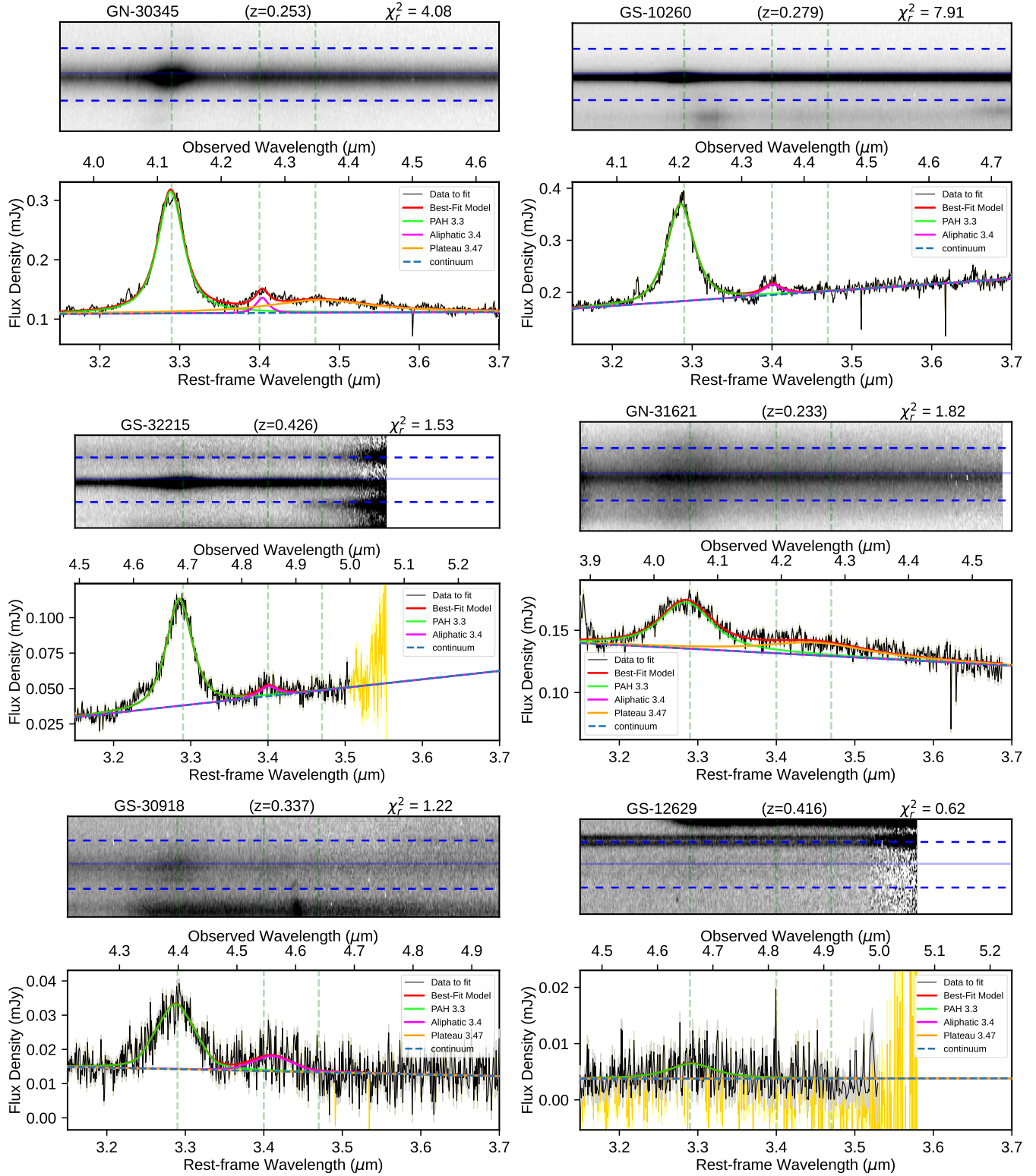


Figure 2. Example FRESKO 2-D spectral images (top) and extracted 1-D spectra (bottom) of example GOODS galaxies with 3.3 μm PAH emission detections. For the 2-D spectral images, we highlight the source center (solid blue line) and $\pm 0.75''$ distance along the dispersion direction (dashed blue line). In the spectral plot, the data used to constrain the model is shown in black lines with gray shades for the $1-\sigma$ flux uncertainties. The orange line with yellow shades are the data and uncertainties dropped for the fittings. The best-fit model for the 1-D spectrum is denoted as a red solid line with the 3.3 μm PAH component in green, 3.4 μm PAH component in magenta, 3.47 μm PAH plateau in orange and the featureless continuum in blue dashed line. The complete figure set (200 images) is available in the online journal.

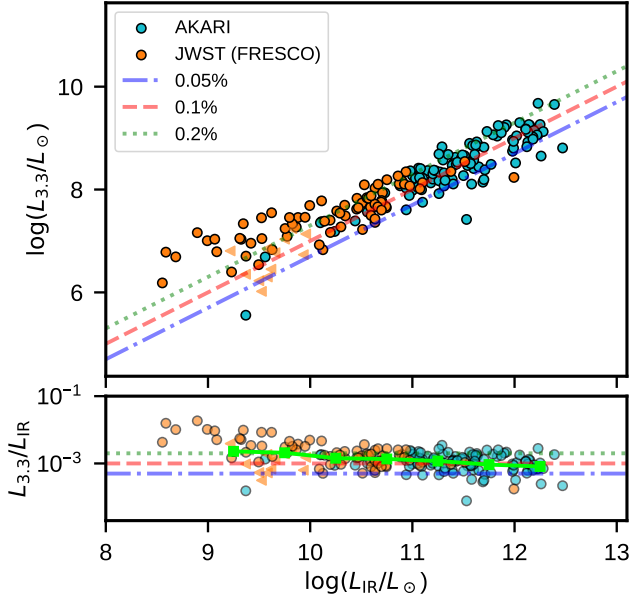


Figure 3. Top panel: Correlation between the galaxy $3.3\,\mu\text{m}$ PAH luminosity ($L_{3.3}$) and IR luminosity (L_{IR}), from our sample (orange dots) and those obtained with AKARI (blue dots). Bottom panel: Variation of $L_{3.3}/L_{\text{IR}}$ with L_{IR} . In both plots, $L_{3.3}/L_{\text{IR}} = 0.0005$, 0.001 , and 0.002 are shown as dot-dashed, dashed and dotted lines, respectively. In bottom panel, the green-square-connected solid line plots the averaged $L_{3.3}/L_{\text{IR}}$ value in different bins of L_{IR} . See text for details.

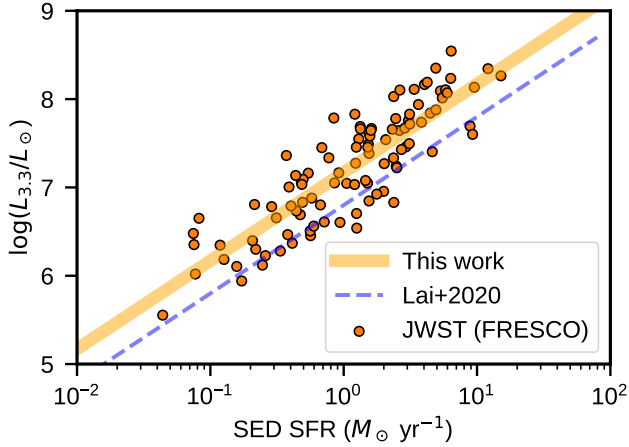


Figure 4. Top panel: Relation between the galaxy $3.3\,\mu\text{m}$ PAH luminosity $L_{3.3}$ and the SED-derived SFR. The orange solid thick line is the fitted correlation in log-log space from this work, and the blue dashed thin line is the $L_{3.3}$ –SFR relation presented in Lai et al. (2020).

various measurement uncertainties. For example, the $3.3\,\mu\text{m}$ PAH emission (relative to the IR luminosity) is boosted by a factor of ~ 2 (0.3 dex) in the low IR luminosity range studied here compared to the high luminosity range in Lai et al. (2020). Nevertheless, considering the large calibration uncertainties in these correlations (~ 0.3 – 0.5 dex), such offsets are not very significant, indicating a general agreement. In other words, the $3.3\,\mu\text{m}$ PAH luminosity does effectively trace star formation rates across a wide range from $\sim 0.1\,M_{\odot}\,\text{yr}^{-1}$ to $\sim 300\,M_{\odot}\,\text{yr}^{-1}$.

4.1.3. $L_{3.3}$ vs. Metallicity

Given the role of metallicity in regulating PAH formation and survival, we also explore the dependence of $L_{3.3}/L_{\text{IR}}$ on the gas-phase metallicity, probing potential links between the chemical enrichment and the PAH emission efficiency.

In Figure 5, we show the relative strength of the $3.3\,\mu\text{m}$ PAH emission to the galaxy IR luminosity as a function of galaxy metallicity $12 + \log(\text{O}/\text{H})$ estimated based on FMR. The correlation analysis between $L_{3.3}/L_{\text{IR}}$ and metallicity $12 + \log(\text{O}/\text{H})$ shows a weak but statistically significant monotonic relationship. The Spearman correlation ($\rho \approx 0.21$, $p \approx 0.032$) and Kendall’s tau ($\tau \approx 0.14$, $p \approx 0.043$) indicate that as the metallicity increases, $L_{3.3}/L_{\text{IR}}$ tends to increase, though the trend is weak. After binning the data points by metallicity, we can clearly see a drop at lower metallicities, regardless of whether the non-detections are considered or not. The change happens at $12 + \log(\text{O}/\text{H}) \sim 8.4$ – 8.5 , corresponding to $\sim 60\%$ – 80% solar metallicity. This trend is roughly consistent with previous studies of other PAH bands in the mid-IR obtained with *Spitzer* such as Draine & Li (2007); Marble et al. (2010) and Whitcomb et al. (2024), including galaxies at redshifts up to ~ 2 (Shivaei et al. 2024).

The exact reason for the deficiency of PAHs in low-metallicity galaxies is not clear (see Li 2020). It is generally interpreted as more rapid destruction of PAHs by the more intense and harder UV radiation (as indicated by the fine-structure line ratio of $[\text{NeIII}]/[\text{NeII}]$) in an ISM with reduced shielding by dust. Low-metallicity environments lack sufficient dust grains to shield PAHs from photodissociation by UV radiation. It could also be due to more effective destruction of PAHs by thermal sputtering in shock-heated gas that cools more slowly because of the reduced metallicity (see Li 2020).

The trend of $L_{3.3}/L_{\text{IR}}$ increasing with metallicity can also be explained by the delayed enrichment of PAHs in the ISM, as highlighted by Galliano et al. (2008). In low-metallicity galaxies, the primary contributors to PAH production—carbon-rich asymptotic giant branch (AGB) stars—take hundreds of millions of years to evolve and inject PAHs into the ISM. As a result, young, metal-poor galaxies experience a

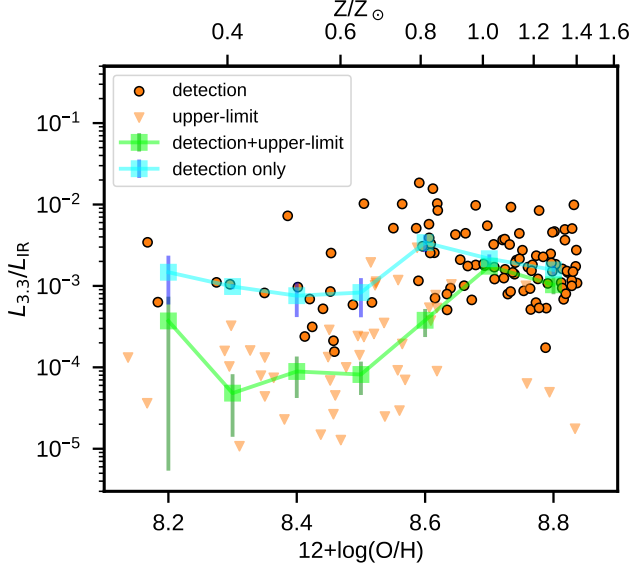


Figure 5. The galaxy 3.3 μm PAH emission relative to the total IR luminosity ($L_{3.3}/L_{\text{IR}}$) as a function of galaxy metallicity $12 + \log(\text{O}/\text{H})$ inferred from the FMR. We computed the average values of $L_{3.3}/L_{\text{IR}}$ in different bins of $12 + \log(\text{O}/\text{H})$ for sources with 3.3 μm PAH detections only (blue squares) and sources with both detections and upper limits (green squares). To compute mean values with measurements that include upper limits, we used the Kaplan-Meier analysis.

deficit in PAH emission, leading to lower $L_{3.3}/L_{\text{IR}}$ ratios. In contrast, higher-metallicity galaxies, which have undergone more extensive star formation and stellar evolution, benefit from the cumulative contribution of AGB stars, enriching the ISM with PAHs over time. This enrichment boosts the PAH emission relative to the total IR luminosity. The increasing $L_{3.3}/L_{\text{IR}}$ ratio at higher metallicities reflects the more developed carbon chemistry in these galaxies, where PAH formation and survival are favored. This evolutionary process, coupled with the reduced destruction of PAHs in less harsh radiation environments of mature galaxies, naturally explains the observed metallicity dependence of $L_{3.3}/L_{\text{IR}}$.

4.2. The 3.4 μm Aliphatic Band

As mentioned earlier, the 3.4 μm emission band provides insight into the aliphatic component of PAH molecules. We now turn to the analysis of this weaker yet crucial feature to further explore the composition and processing of PAHs in galaxies.

For galaxies with both the 3.3 μm aromatic and 3.4 μm aliphatic features detected at 3- σ significance, a large variation of the aliphatic-to-aromatic band ratio ($P_{3.4}/P_{3.3}$) is observed from ~ 0.05 to ~ 0.58 , with a mean value of ~ 0.22 (and a standard deviation of ~ 0.14) and a median value of ~ 0.19 . As discussed in Yang & Li (2023), the aliphatic frac-

tions (η_{ali}) of PAHs, defined as the fractions of C atoms in aliphatic units, can be determined from the 3.4 μm -to-3.3 μm emission intensity ratios ($P_{3.4}/P_{3.3}$):

$$\eta_{\text{ali}} = (1 + N_{\text{C,aro}}/N_{\text{C,ali}})^{-1}, \quad (6)$$

$$\frac{N_{\text{C,ali}}}{N_{\text{C,aro}}} \approx \frac{1}{6.40} \left(\frac{P_{3.4}}{P_{3.3}} \right), \quad (7)$$

where $N_{\text{C,aro}}$ and $N_{\text{C,ali}}$ are respectively the number of aromatic and aliphatic C atoms in a PAH molecule. In the FRESCO galaxies considered here, the observed $P_{3.4}/P_{3.3}$ ratios translate into aliphatic fractions of η_{ali} from $\sim 0.78\%$ to $\sim 8.3\%$, with a mean value of $\sim 3.3\%$ (and a standard deviation of $\sim 1.9\%$) and a median value of $\sim 2.9\%$. As the PAH aliphatic fraction η_{ali} is linearly related to $P_{3.4}/P_{3.3}$, provided $N_{\text{C,ali}} \ll N_{\text{C,aro}}$ (see eqs. 6, 7), in the following we will discuss the PAH aliphaticity simply in terms of $P_{3.4}/P_{3.3}$ or $L_{3.4}/L_{3.3}$, where $L_{3.3} = P_{3.3} \times 4\pi \times D^2$, $L_{3.4} = P_{3.4} \times 4\pi \times D^2$, and D is the luminosity distance to the galaxy.

In Figure 6, we compare the observed aliphatic fraction measured as $L_{3.4}/L_{3.3}$, the ratio of the 3.3 μm luminosity to the 3.4 μm luminosity, to various galaxy properties such as redshift, stellar mass, metallicity, and star formation rate, and conduct various correlation tests (Pearson, Spearman, and Kendall). We discuss the results and implications below.

4.2.1. PAH Aliphaticity vs. Redshift

We plot the aliphaticity of PAHs (measured as $L_{3.4}/L_{3.3}$) versus redshift in the top-left panel of Figure 6. All the correlation tests conclude a near zero correlation. In other words, the PAH aliphaticity in galaxies does not evolve within the observed redshift range.

The lack of redshift dependence of the PAH aliphaticity suggests that the balance between aliphaticization and aromatization of PAHs is influenced more by local galactic conditions than by cosmic evolution. This stability spans the redshift range of $z \sim 0.2$ – 0.5 , corresponding to a cosmic time of about 2.5 to 5 billion years ago. PAH processing timescales, including formation, evolution, and destruction, are relatively short, often occurring over timescales of 10^6 to 10^8 yr, depending on environmental factors such as UV radiation intensity and the presence of shocks. For instance, in hot gas environments, PAH lifetimes can be as short as a few thousand years due to collisions with energetic particles (Micelotta et al. 2010a). In interstellar shocks, PAHs can be destroyed on timescales of a few hundred million years (Micelotta et al. 2010b). These relatively rapid processing timescales allow PAH populations to reach equilibrium states that reflect local conditions, leading to the observed consistency in $L_{3.4}/L_{3.3}$ across different redshifts.

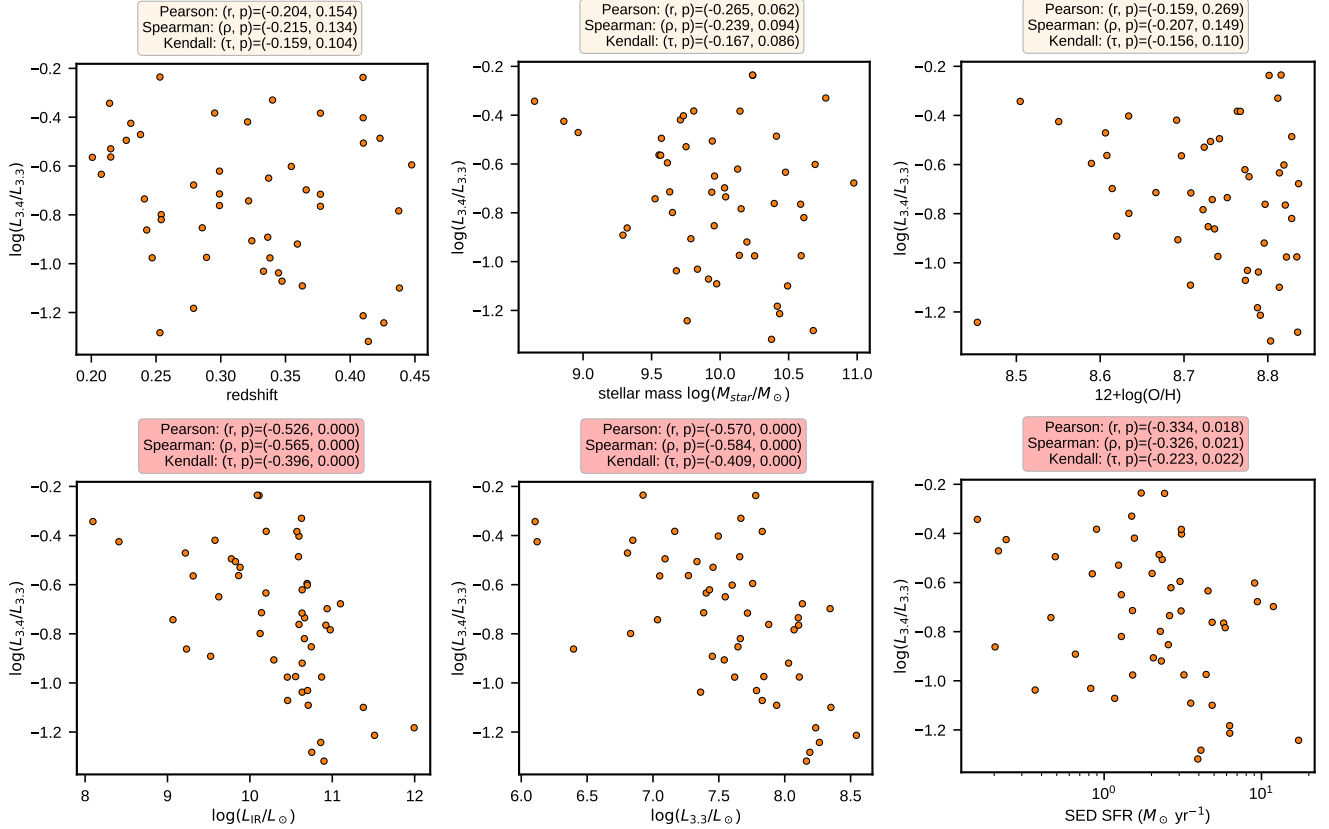


Figure 6. The aliphatic fraction of PAHs (measured as $L_{3.4}/L_{3.3}$) as functions of various galaxy properties (i.e., redshift, stellar mass, metallicity, and star formation rate measured from L_{IR} , $L_{3.3}$ and SED). We denote the correlation coefficients and P -values of Pearson, Spearman, Kendall in the text box.

4.2.2. PAH Aliphaticity vs. Stellar Mass

Stellar mass serves as a fundamental tracer of galaxy evolution, correlating with properties such as star formation history, dust content, and ISM conditions, which may influence PAH spectral variations. More massive galaxies tend to have older stellar populations, different ISM environments, and a higher dust-to-gas ratio, all of which could impact the balance between aromatic and aliphatic PAH emission. Additionally, given that PAHs are sensitive to local radiation fields, variations in stellar populations across different mass regimes might affect PAH processing, including hydrogenation and dehydrogenation cycles. If the 3.4/3.3 PAH ratio were linked to the bulk properties of a galaxy, a dependence on stellar mass might be expected, providing insight into the role of large-scale galactic structure in shaping PAH emission.

However, as shown in the upper middle panel in Figure 6, there is no significant correlation between the 3.4/3.3 PAH ratio and stellar mass, indicating that the global galaxy properties do not play a dominant role in regulating this ratio.

4.2.3. PAH Aliphaticity vs. Metallicity

In principle, the aliphatic fractions of PAHs in galaxies could be related to the galaxy metallicity. If the 3.4 μm emission band indeed arises from the aliphatic sidegroups (e.g., $-\text{CH}_3$ and $-\text{CH}_2-$) attached to PAHs, one may expect a lower aliphatic fraction (i.e., a lower $L_{3.4}/L_{3.3}$ ratio) in galaxies with lower metallicities. This is because, as discussed earlier in §4.1.3, in low-metallicity galaxies the starlight radiation is harder and more intense due to the reduced shielding by dust. In such hostile environments, the aliphatic sidegroups are more likely stripped off from the parent PAH molecules by UV photons and therefore one expects a lower PAH aliphaticity. However, as shown in the top-right panel of Figure 6, we basically see no correlation between the aliphaticity and the galaxy metallicity.

Alternatively, the 3.4 μm band could originate from super-hydrogenated PAHs whose edges contain excess H atoms, i.e., some peripheral C atoms have two H atoms. The extra H atom converts the originally aromatic ring into an aliphatic ring and creates two aliphatic C–H stretches that may be responsible for the 3.4 μm feature (Bernstein et al. 1996; Sandford et al. 2013; Steglich et al. 2013; Yang et al. 2020). In this case, in low metallicity environments (with a low C/H abundance), there are plenty of H atoms available to super-

hydrogenate a PAH molecule. Therefore, one would expect a higher aliphatic fraction for PAHs in low-metallicity galaxies. However, we do not see in Figures 6 any appreciable increase of $L_{3.4}/L_{3.3}$ toward low metallicity.

On the other hand, the $3.4\ \mu\text{m}$ emission feature could also be (partly) due to the anharmonicity of the aromatic C–H stretches (see Barker et al. 1987; Maltseva et al. 2016). In a harmonic oscillator, the spacing between all adjacent vibrational energy levels is constant, hence the $\Delta v = 1$ vibrational transitions between high v levels result in the same spectral line as that of the $v = 1 \rightarrow 0$ transition (where v is the vibrational quantum number). In contrast, anharmonicity would continuously decrease the spacing between the adjacent vibrational states for higher values of v , and therefore the $\Delta v = 1$ transitions between higher v levels occur at increasingly longer wavelengths. The anharmonicity hypothesis interprets the weaker feature at $3.4\ \mu\text{m}$ as the $v = 2 \rightarrow 1$ “hot band” of the $3.3\ \mu\text{m}$ fundamental $v = 1 \rightarrow 0$ aromatic C–H stretching mode (see Barker et al. 1987).

The exact origin of the $3.4\ \mu\text{m}$ band is currently under debate (see Yang et al. 2017b; Tokunaga & Bernstein 2021). A more thorough exploration of the PAH aliphaticity and its variation with physical and chemical conditions would provide valuable insights into the nature of this band. It would be interesting, for example, to examine the 3.3 and $3.4\ \mu\text{m}$ emission bands in the Small Magellanic Cloud (SMC) where the metallicity is lower than that of the Galactic ISM by a factor of ~ 5 (e.g., see Li & Draine 2002).

4.2.4. PAH Aliphaticity vs. SFR

To explore how star formation influences the balance between the aromatization and aliphaticization of PAHs, we now examine the relationship between $L_{3.4}/L_{3.3}$ and various star-formation indicators.

As shown in the bottom panels in Figure 6, there are clear negative correlations between $L_{3.4}/L_{3.3}$ and all three star-formation indicators (i.e., L_{IR} , $L_{3.3}$, and SED-derived SFR). The p -values of all three tests are well below the typical threshold of 0.05, indicating the correlations are statistically significant.

These results suggest that the aliphatic C–H bonds are sensitive to photodissociation in UV-rich environments, e.g., UV photons from active star-forming regions preferentially strip off the aliphatic sidegroups from PAH molecules (Allamandola et al. 1985; Tielens 2008). This aligns with experimental studies showing that aliphatic bonds are less stable and more prone to UV-induced dissociation compared to aromatic C–H bonds (e.g., Sandford et al. 2013). Lai et al. (2020) adopted the continuum slope between 15 and $30\ \mu\text{m}$ to trace the intensity of the radiation field and reported a weak trend of decreasing $L_{3.4}/L_{3.3}$ with the increasing of radiation field. In comparison, our results are statistically more significant.

The suppression of PAH aliphaticity in galaxies with intense star formation suggests that PAH composition traces local UV radiation fields. In active star-forming regions, lower $L_{3.4}/L_{3.3}$ reflects the preferential destruction of aliphatic bonds by UV photons, while more quiescent environments preserve these bonds. This highlights how PAH restructuring is driven by UV processing rather than metallicity or global galaxy properties. The resilience of aromatic C–H bonds in UV-dominated regions explains the consistent detection of the $3.3\ \mu\text{m}$ band across diverse galaxy types and redshifts, reinforcing its value as a tracer of star formation in harsh environments (e.g., Tielens 2008; Kim et al. 2012; Tacconi-Garman & Sturm 2013). The $L_{3.4}/L_{3.3}$ ratio thus offers insight into the interplay between UV radiation, ISM chemistry, and star formation activity over cosmic time.

4.2.5. PAH Aliphaticity vs. Galaxy Morphology

We now investigate the detection rates of the 3.3 and $3.4\ \mu\text{m}$ PAH emission bands in galaxies of different morphological types, including undisturbed disks, disturbed disks, spheroids, point sources, irregulars, and mergers. A contingency table was constructed to compare the detection of the 3.3 and $3.4\ \mu\text{m}$ features across these six morphology categories. We applied a chi-square test to assess whether the detection frequencies depend on morphology. The results, as shown in Figure 7, yield p -values of ~ 0.167 for the $3.3\ \mu\text{m}$ feature and ~ 0.511 for the $3.4\ \mu\text{m}$ feature—both exceeding the 0.05 threshold, indicating no statistically significant difference in PAH detection rates across different galaxy morphologies.

To further explore potential trends, we examine the distribution of $L_{3.4}/L_{3.3}$ across the same morphological classifications, as shown in Figure 8. Although there is considerable scatter, the overall distribution of $L_{3.4}/L_{3.3}$ appears similar across different morphological types, suggesting no strong dependence on galaxy morphology.

These results suggest that the physical processes regulating the balance between PAH aromatization and aliphaticization are largely independent of large-scale structural features. The lack of correlation implies that the local star-formation activities, rather than the galaxy global morphology, dominate the PAH chemical structure. This is consistent with the idea that the UV radiation fields, driven by localized star formation, primarily modify PAH composition, regardless of whether the host galaxy is a merger, disk, or irregular system.

While mergers and irregulars exhibit a slightly broader range of $L_{3.4}/L_{3.3}$ ratios, this likely reflects the diversity of star formation activities within these systems rather than morphological influences. Overall, the uniformity in $L_{3.4}/L_{3.3}$ ratios across different morphologies highlights the robustness of PAH emission as tracers of star formation and UV processing, regardless of galaxy types.

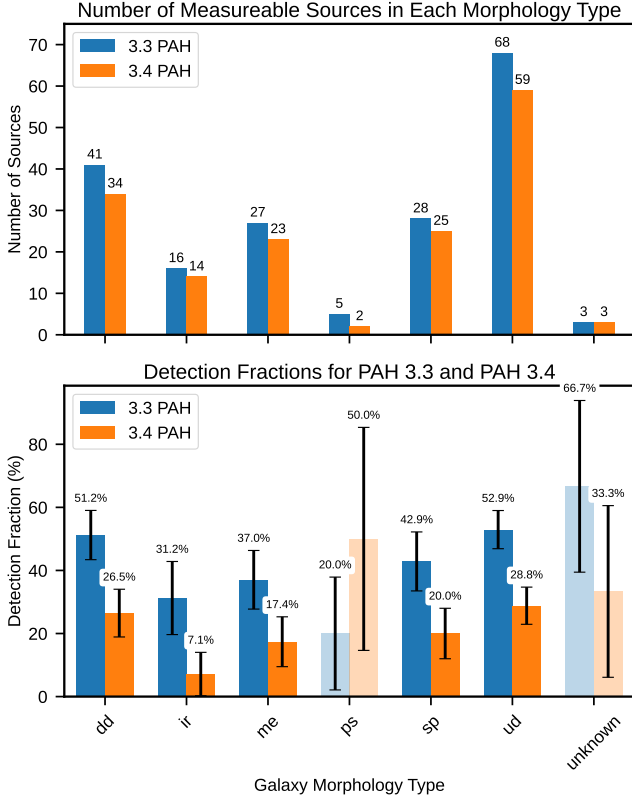


Figure 7. Top panel: Histograms of sources with useful NIRCam/WFSS data to determine the 3.3 and 3.4 μm emission against galaxy morphology type. Bottom panel: Detection rates of the PAH 3.3 and 3.4 μm emission bands among different galaxy morphology types.

5. SUMMARY

We have presented a comprehensive survey for the 3.3 μm aromatic and 3.4 μm aliphatic C–H stretching emission of PAHs in 200 galaxies at $z \sim 0.2\text{--}0.5$ using JWST/NIRCam WFSS data from the JWST Cycle 1 legacy program FRESCO. This study extends the detection and characterization of these PAH features well beyond the local Universe, probing galaxies with IR luminosities as low as $L_{\text{IR}} \sim 10^9\text{--}10^{10} L_{\odot}$, significantly lower than in previous extragalactic PAH studies from e.g., AKARI or *Spitzer*. Our major results are:

1. In terms of detections, the 3.3 μm aromatic feature is detected in 88 of 187 galaxies and the 3.4 μm aliphatic feature is detected in 37 of 159 galaxies. Sources without detections are mostly due to their weak PAH emission which fails below the NIRCam/WFSS detection limit;
2. The 3.3 μm aromatic emission ($L_{3.3}$) is strongly correlated with the galaxy IR luminosity (L_{IR}) over three orders of magnitude. Meanwhile, the relative strength

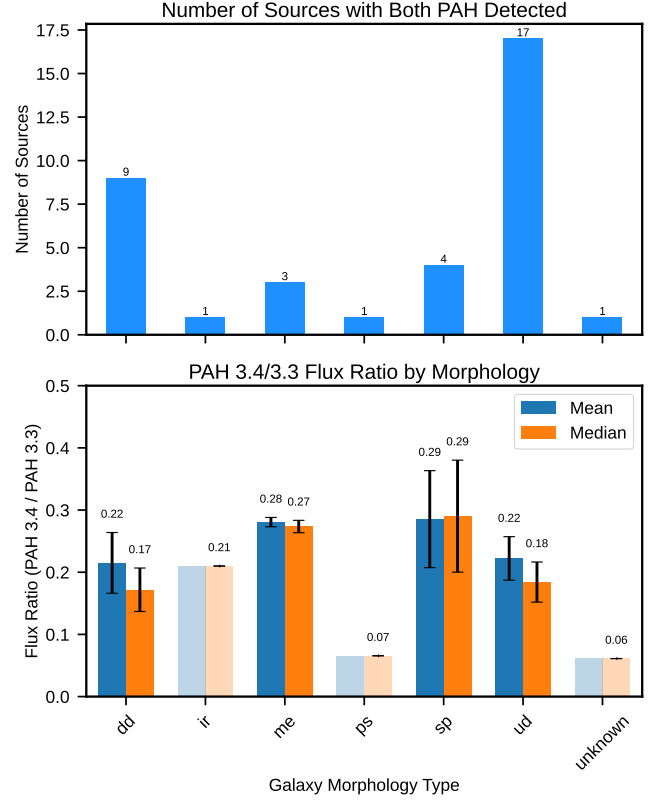


Figure 8. Top panel: Histograms of sources with both the 3.3 and 3.4 μm bands detected against galaxy morphology type. Bottom panel: the mean and median values of $L_{3.4}/L_{3.3}$ by morphology types.

of this feature to the galaxy IR luminosity ($L_{3.3}/L_{\text{IR}}$) shows a strong dependence on galaxy metallicity, with lower metallicity galaxies exhibiting weaker PAH emission;

3. The 3.3 μm aromatic emission strength is also closely correlated with the SFRs derived either from the galaxy IR luminosity or from the galaxy SED. We have demonstrated that the 3.3 μm PAH emission is a valid SFR indicator (see Equation 5) for galaxies with a broad range of SFRs from $\sim 0.1 M_{\odot} \text{yr}^{-1}$ to $\sim 300 M_{\odot} \text{yr}^{-1}$ with an intrinsic scatter of $\sim 0.2\text{--}0.3$ dex. This tight correlation establishes the usage of the 3.3 μm PAH emission to infer SFRs in large statistical samples of galaxies across cosmic time with JWST and future IR telescopes;
4. The ratios of the 3.4 and 3.3 μm PAH emission ($L_{3.4}/L_{3.3}$) show a range of variations from ~ 0.05 to ~ 0.58 , with a median value at ~ 0.19 , indicating PAH aliphatic fractions (measured as the fractions of carbon atoms in aliphatic units) of $\sim 0.78\%\text{--}8.3\%$ with a median value of $\sim 2.9\%$. A negative correlation be-

tween $L_{3.4}/L_{3.3}$ and the SFR indicators (e.g., L_{IR} , $L_{3.3}$, and SED-derived SFR) suggests that UV photons from active star-forming regions strip off the aliphatic sidegroups from PAH molecules;

5. We do not detect any significant evolution of PAH aliphatic fractions (as measured by $L_{3.4}/L_{3.3}$) with galaxy redshift, stellar mass, metallicity, or morphology, indicating that the aliphatic component of PAHs is more sensitive to local star formation conditions than to global galaxy properties.

Our work demonstrates the power of the JWST NIRCam/WFSS mode in surveying PAH molecules in statistically significant, less-biased samples of galaxies, providing a more comprehensive view of PAH properties and star formation processes across cosmic time. This study paves the way for future programs to explore the nature, origin and evolution of PAHs and their role in galaxy formation beyond the local Universe.

JL is supported in part by JWST Mid-Infrared Instrument (MIRI) grant No. 80NSSC18K0555, and the NIRCam science support contract NAS5-02105, both from NASA Goddard Space Flight Center to the University of Arizona; AL is supported in part by STScI Award JWST-AR-03879.001-A. XJY is supported in part by NSFC 12333005 and 12122302.

This work is based on observations made with the NASA/ESA/CSA James Webb Space Telescope. The data were obtained from the Mikulski Archive for Space Telescopes at the Space Telescope Science Institute, which is operated by the Association of Universities for Research in Astronomy, Inc., under NASA contract NAS 5-03127 for JWST. These observations are associated with program 1895 (FRESCO). The authors acknowledge the FRESCO team for developing their observing program with a zero-exclusive-access period.

Facilities: JWST (NIRCam)

Software: Astropy (Astropy Collaboration et al. 2018), Matplotlib (Hunter 2007), NumPy (Harris et al. 2020), SciPy (Virtanen et al. 2020)

REFERENCES

- Alberts, S., Lyu, J., Shivaee, I., et al. 2024, ApJ, 976, 224, doi: [10.3847/1538-4357/ad7396](https://doi.org/10.3847/1538-4357/ad7396)
- Allamandola, L. J., Boersma, C., Lee, T. J., Bregman, J. D., & Temi, P. 2021, ApJL, 917, L35, doi: [10.3847/2041-8213/ac17f0](https://doi.org/10.3847/2041-8213/ac17f0)
- Allamandola, L. J., Tielens, A. G. G. M., & Barker, J. R. 1985, ApJL, 290, L25, doi: [10.1086/184435](https://doi.org/10.1086/184435)
- Astropy Collaboration, Price-Whelan, A. M., Sipőcz, B. M., et al. 2018, AJ, 156, 123, doi: [10.3847/1538-3881/aabc4f](https://doi.org/10.3847/1538-3881/aabc4f)
- Barker, J. R., Allamandola, L. J., & Tielens, A. G. G. M. 1987, ApJL, 315, L61, doi: [10.1086/184861](https://doi.org/10.1086/184861)
- Bernstein, M. P., Sandford, S. A., & Allamandola, L. J. 1996, ApJL, 472, L127, doi: [10.1086/310376](https://doi.org/10.1086/310376)
- Draine, B. T., & Li, A. 2007, ApJ, 657, 810, doi: [10.1086/511055](https://doi.org/10.1086/511055)
- Draine, B. T., Li, A., Hensley, B. S., et al. 2021, ApJ, 917, 3, doi: [10.3847/1538-4357/abff51](https://doi.org/10.3847/1538-4357/abff51)
- Elbaz, D., Dickinson, M., Hwang, H. S., et al. 2011, A&A, 533, A119, doi: [10.1051/0004-6361/201117239](https://doi.org/10.1051/0004-6361/201117239)
- Galliano, F., Dwek, E., & Chianial, P. 2008, ApJ, 672, 214, doi: [10.1086/523621](https://doi.org/10.1086/523621)
- Geballe, T. R., Joblin, C., D’Hendecourt, L. B., et al. 1994, ApJL, 434, L15, doi: [10.1086/187561](https://doi.org/10.1086/187561)
- Gregg, B., Calzetti, D., Adamo, A., et al. 2024, arXiv e-prints, arXiv:2405.09667, doi: [10.48550/arXiv.2405.09667](https://doi.org/10.48550/arXiv.2405.09667)

- Harris, C. R., Millman, K. J., van der Walt, S. J., et al. 2020, *Nature*, 585, 357, doi: [10.1038/s41586-020-2649-2](https://doi.org/10.1038/s41586-020-2649-2)
- Hinshaw, G., Larson, D., Komatsu, E., et al. 2013, *ApJS*, 208, 19, doi: [10.1088/0067-0049/208/2/19](https://doi.org/10.1088/0067-0049/208/2/19)
- Horne, K. 1986, *PASP*, 98, 609, doi: [10.1086/131801](https://doi.org/10.1086/131801)
- Hunter, J. D. 2007, *Computing in Science and Engineering*, 9, 90, doi: [10.1109/MCSE.2007.55](https://doi.org/10.1109/MCSE.2007.55)
- Ichikawa, K., Imanishi, M., Ueda, Y., et al. 2014, *ApJ*, 794, 139, doi: [10.1088/0004-637X/794/2/139](https://doi.org/10.1088/0004-637X/794/2/139)
- Imanishi, M., Nakagawa, T., Shirahata, M., Ohyama, Y., & Onaka, T. 2010, *ApJ*, 721, 1233, doi: [10.1088/0004-637X/721/2/1233](https://doi.org/10.1088/0004-637X/721/2/1233)
- Johnson, B. D., Leja, J., Conroy, C., & Speagle, J. S. 2021, *ApJS*, 254, 22, doi: [10.3847/1538-4365/abef67](https://doi.org/10.3847/1538-4365/abef67)
- Kennicutt, Robert C., J. 1998, *ARA&A*, 36, 189, doi: [10.1146/annurev.astro.36.1.189](https://doi.org/10.1146/annurev.astro.36.1.189)
- Kennicutt, R. C., & Evans, N. J. 2012, *ARA&A*, 50, 531, doi: [10.1146/annurev-astro-081811-125610](https://doi.org/10.1146/annurev-astro-081811-125610)
- Kim, J. H., Im, M., Lee, H. M., et al. 2012, *ApJ*, 760, 120, doi: [10.1088/0004-637X/760/2/120](https://doi.org/10.1088/0004-637X/760/2/120)
- Kobulnicky, H. A., & Kewley, L. J. 2004, *ApJ*, 617, 240, doi: [10.1086/425299](https://doi.org/10.1086/425299)
- Kocevski, D. D., Brightman, M., Nandra, K., et al. 2015, *ApJ*, 814, 104, doi: [10.1088/0004-637X/814/2/104](https://doi.org/10.1088/0004-637X/814/2/104)
- Kriek, M., & Conroy, C. 2013, *ApJL*, 775, L16, doi: [10.1088/2041-8205/775/1/L16](https://doi.org/10.1088/2041-8205/775/1/L16)
- Lai, T. S. Y., Smith, J. D. T., Baba, S., Spoon, H. W. W., & Imanishi, M. 2020, *ApJ*, 905, 55, doi: [10.3847/1538-4357/abc002](https://doi.org/10.3847/1538-4357/abc002)
- Leger, A., & Puget, J. L. 1984, *A&A*, 137, L5
- Leja, J., Johnson, B. D., Conroy, C., van Dokkum, P. G., & Byler, N. 2017, *ApJ*, 837, 170, doi: [10.3847/1538-4357/aa5ffe](https://doi.org/10.3847/1538-4357/aa5ffe)
- Li, A. 2020, *Nature Astronomy*, 4, 339, doi: [10.1038/s41550-020-1051-1](https://doi.org/10.1038/s41550-020-1051-1)
- Li, A., & Draine, B. T. 2002, *ApJ*, 576, 762, doi: [10.1086/341796](https://doi.org/10.1086/341796)
- Lyu, J., Alberts, S., Rieke, G. H., & Rujopakarn, W. 2022, *ApJ*, 941, 191, doi: [10.3847/1538-4357/ac9e5d](https://doi.org/10.3847/1538-4357/ac9e5d)
- Lyu, J., & Rieke, G. H. 2017, *ApJ*, 841, 76, doi: [10.3847/1538-4357/aa7051](https://doi.org/10.3847/1538-4357/aa7051)
- Lyu, J., Alberts, S., Rieke, G. H., et al. 2024, *ApJ*, 966, 229, doi: [10.3847/1538-4357/ad3643](https://doi.org/10.3847/1538-4357/ad3643)
- Maltseva, E., Petrignani, A., Candian, A., et al. 2016, *ApJ*, 831, 58, doi: [10.3847/0004-637X/831/1/58](https://doi.org/10.3847/0004-637X/831/1/58)
- Marble, A. R., Engelbracht, C. W., van Zee, L., et al. 2010, *ApJ*, 715, 506, doi: [10.1088/0004-637X/715/1/506](https://doi.org/10.1088/0004-637X/715/1/506)
- Micelotta, E. R., Jones, A. P., & Tielens, A. G. G. M. 2010a, *A&A*, 510, A37, doi: [10.1051/0004-6361/200911683](https://doi.org/10.1051/0004-6361/200911683)
- . 2010b, *A&A*, 510, A36, doi: [10.1051/0004-6361/200911682](https://doi.org/10.1051/0004-6361/200911682)
- Oesch, P. A., Brammer, G., Naidu, R. P., et al. 2023, *MNRAS*, 525, 2864, doi: [10.1093/mnras/stad2411](https://doi.org/10.1093/mnras/stad2411)
- Pillari, P., Joblin, C., Boulanger, F., & Onaka, T. 2015, *A&A*, 577, A16, doi: [10.1051/0004-6361/201425590](https://doi.org/10.1051/0004-6361/201425590)
- Pope, A., Chary, R.-R., Alexander, D. M., et al. 2008, *ApJ*, 675, 1171, doi: [10.1086/527030](https://doi.org/10.1086/527030)
- Rieke, G. H., Alonso-Herrero, A., Weiner, B. J., et al. 2009, *ApJ*, 692, 556, doi: [10.1088/0004-637X/692/1/556](https://doi.org/10.1088/0004-637X/692/1/556)
- Rujopakarn, W., Rieke, G. H., Weiner, B. J., et al. 2013, *ApJ*, 767, 73, doi: [10.1088/0004-637X/767/1/73](https://doi.org/10.1088/0004-637X/767/1/73)
- Sanders, R. L., Shapley, A. E., Jones, T., et al. 2021, *ApJ*, 914, 19, doi: [10.3847/1538-4357/abf4c1](https://doi.org/10.3847/1538-4357/abf4c1)
- Sandford, S. A., Bernstein, M. P., & Materese, C. K. 2013, *ApJS*, 205, 8, doi: [10.1088/0067-0049/205/1/8](https://doi.org/10.1088/0067-0049/205/1/8)
- Sandstrom, K. M., Chastenet, J., Sutter, J., et al. 2023, *ApJL*, 944, L7, doi: [10.3847/2041-8213/acb0cf](https://doi.org/10.3847/2041-8213/acb0cf)
- Shipley, H. V., Papovich, C., Rieke, G. H., Brown, M. J. I., & Moustakas, J. 2016, *ApJ*, 818, 60, doi: [10.3847/0004-637X/818/1/60](https://doi.org/10.3847/0004-637X/818/1/60)
- Shivaei, I., Alberts, S., Florian, M., et al. 2024, *arXiv e-prints*, arXiv:2402.07989, doi: [10.48550/arXiv.2402.07989](https://doi.org/10.48550/arXiv.2402.07989)
- Skelton, R. E., Whitaker, K. E., Momcheva, I. G., et al. 2014, *ApJS*, 214, 24, doi: [10.1088/0067-0049/214/2/24](https://doi.org/10.1088/0067-0049/214/2/24)
- Spilker, J. S., Phadke, K. A., Aravena, M., et al. 2023, *Nature*, 618, 708, doi: [10.1038/s41586-023-05998-6](https://doi.org/10.1038/s41586-023-05998-6)
- Steglich, M., Jäger, C., Huisken, F., et al. 2013, *ApJS*, 208, 26, doi: [10.1088/0067-0049/208/2/26](https://doi.org/10.1088/0067-0049/208/2/26)
- Sun, F., Egami, E., Pirzkal, N., et al. 2023, *ApJ*, 953, 53, doi: [10.3847/1538-4357/acd53c](https://doi.org/10.3847/1538-4357/acd53c)
- Tacconi-Garman, L. E., & Sturm, E. 2013, *A&A*, 551, A139, doi: [10.1051/0004-6361/201220642](https://doi.org/10.1051/0004-6361/201220642)
- Tielens, A. G. G. M. 2008, *ARA&A*, 46, 289, doi: [10.1146/annurev.astro.46.060407.145211](https://doi.org/10.1146/annurev.astro.46.060407.145211)
- Tokunaga, A. T., & Bernstein, L. S. 2021, *ApJ*, 916, 52, doi: [10.3847/1538-4357/ac004b](https://doi.org/10.3847/1538-4357/ac004b)
- Virtanen, P., Gommers, R., Oliphant, T. E., et al. 2020, *Nature Methods*, 17, 261, doi: [10.1038/s41592-019-0686-2](https://doi.org/10.1038/s41592-019-0686-2)
- Whitcomb, C. M., Smith, J. D. T., Sandstrom, K., et al. 2024, *ApJ*, 974, 20, doi: [10.3847/1538-4357/ad66c8](https://doi.org/10.3847/1538-4357/ad66c8)
- Xie, Y., & Ho, L. C. 2019, *ApJ*, 884, 136, doi: [10.3847/1538-4357/ab4200](https://doi.org/10.3847/1538-4357/ab4200)
- Yang, X. J., Glaser, R., Li, A., & Zhong, J. X. 2017a, *NewAR*, 77, 1, doi: [10.1016/j.newar.2017.01.001](https://doi.org/10.1016/j.newar.2017.01.001)
- Yang, X. J., & Li, A. 2023, *ApJS*, 268, 50, doi: [10.3847/1538-4365/acebe6](https://doi.org/10.3847/1538-4365/acebe6)
- Yang, X. J., Li, A., & Glaser, R. 2020, *ApJS*, 247, 1, doi: [10.3847/1538-4365/ab67b6](https://doi.org/10.3847/1538-4365/ab67b6)
- Yang, X. J., Li, A., Glaser, R., & Zhong, J. X. 2017b, *ApJ*, 837, 171, doi: [10.3847/1538-4357/aa5fa9](https://doi.org/10.3847/1538-4357/aa5fa9)